Sensors and Actuators Reports 8 (2024) 100211

Contents lists available at ScienceDirect

Sensors and Actuators Reports

journal homepage: www.sciencedirect.com/journal/sensors-and-actuators-reports

Inflammatory biomarker detection in saliva samples by printed graphene immunosensors

D. Vurro [a], L. Pasquardini [b,c,d], M. Borriello [e], R. Foresti [a,f], M. Barra [g], M. Sidoli [h], D. Pontiroli [h], L. Fornasini [h], L. Aversa [c], R. Verucchi [c], P. D'Angelo [a,*], G. Tarabella [a]

[a] Institute of Materials for Electronics and Magnetism, IMEM-CNR, P.co Area delle Scienze 37/A, 43124 Parma, Italy
[b] Indivenire srl, Via Sommarive 18, 38123 Trento, Italy
[c] Institute of Materials for Electronics and Magnetism, IMEM-CNR, Trento site c/o Fondazione Bruno Kessler, Via alla Cascata 56/C, 38123 Trento, Italy
[d] Department of Engineering, University of Campania "Luigi Vanvitelli", Via Roma 29, 81031 Aversa, Italy
[e] Department of Precision Medicine, University of Campania "Luigi Vanvitelli", Via L. De Crecchio 7, 80138 Napoli, Italy
[f] Department of Medicine and Surgery, Via Gramsci, 14 43124, Parma, Italy
[g] CNR-SPIN c/o Department of Physics "Ettore Pancini", P.le Tecchio, 80, 80125 Napoli, Italy
[h] Department of Mathematical, Physical and Computer Sciences, Parco Area delle Scienze, 7/A, 43124 Parma, Italy

ARTICLE INFO

Keywords:
Biosensors
Biomarkers
Saliva samples
Screen printed electrodes
Graphene
Aerosol jet printing
Cytokines storm

ABSTRACT

Herein, we present the design and fabrication of a portable biochemical sensor based on the Screen Printed Electrode (SPE) concept and applied for detecting interleukin-6 (IL-6), a key player in the complex process of inflammation, in real human saliva. The sensing mechanism relies on the antigen-antibody binding between the IL-6 molecule and its antibody immobilized over a surface of a Thermally Exfoliated Graphene Oxide (TEGO) layer. TEGO, deposited by Aerosol Jet Printing (AJP), provides advantages in terms of a time/cost consuming~~fast~~, easy and efficient biofunctionalization. The biosensor shows a dynamic range comprising IL-6 concentrations falling within the normal IL-6 levels in saliva. An extensive analysis of device performance, focused on the assessment of the sensor Limit of Detection (LoD) by two modes (i.e. from the lin-log calibration curve and from blank measurements), provides a best value of about 1×10^{-2} pg/ml of IL-6 in saliva. Our work aims at providing a contribution toward applications in real environment, going beyond a proof of concept or prototyping at lab scale. Hence, the characterization of the sensor was finalized to find a reliable device-to-device reproducibility and calibration through the introduction of a measurement protocol based on comparative measurements between saliva samples without (blank) and with IL-6 spiked in it, in place of the *standard addition method* used in daily laboratory practice. Device-to-device reproducibility has been accordingly tested by acquiring multiple experimental points along the calibration curve using different individual devices for each point.

1. Introduction

Cytokines are small molecules of 10−70 kDa in weight, whose concentration in blood or saliva can be a fingerprint of an inflammatory state in human body. Among the cytokines, the Interleukin-6 (IL-6) family plays an important role as inflammatory marker in the context of several diseases [1]. IL-6 has been also proposed as an informative marker for Covid-19 during pandemic [2]. Its concentration values in saliva falling in the range between 1 and 5 pg/mL are indicative of a healthy state, while an increase in concentration can be associated to an in-progress inflammatory state [3]. Higher IL-6 concentrations can address illness states, for example values of 200–300 pg/mL are indicative of a severe state of inflammation, referred to as "cytokine storm" during pandemic [4]. The quantification of interleukins is generally made by ELISA assays, with the requirement of specialized laboratories and qualified staff. The ability for providing an indicative quantification of cytokine levels in biological matrices by means of user-friendly diagnostic devices may be of useful support under a clinical framework of prevention. Leveraged by pandemic, worldwide research on fast, reliable and portable biochemical electronic sensors exploded in number and in quality, and literature provides a number of designed sensing devices with high potential [5,6], as well as many

* Corresponding author.
E-mail address: pasquale.dangelo@cnr.it (P. D'Angelo).

https://doi.org/10.1016/j.snr.2024.100211
Received 20 December 2023; Received in revised form 1 June 2024; Accepted 5 June 2024
Available online 15 June 2024

proof-of-concept trials [7,8]. A pivotal role for the implementation of bioelectronic sensors is given by the use of solution processable, conducting organic materials, but also carbon-based materials are largely used to this purpose [9]. Accordingly, electrolyte-gated transistors and electrochemical electrodes (i.e. Screen Printed Electrodes, SPEs, and interdigitated electrochemical electrodes, IDEs) implemented using these materials, have been designed and applied as electroanalytical tools for biosensing [10]. SPEs are portable, disposable and user-friendly tools for a rapid detection by analyzing small sample volumes (if required, directly in the field), also providing performance comparable to that of laboratory methods.

SPEs' main interface, i.e. the working electrode (WE), is generally decorated by a recognition element, such as a ligand (e.g. antibody, aptamer, nanobody), that is responsible for the specificity of the device. Then, with the aim of calibrating the SPE, obtaining a dose-response curve, the device is incubated with known concentrations of the desired biomarkers in the appropriate biological matrix, thus reducing the matrix-associated signals. A screening effect at the WE towards the charge transfer efficiency in presence of an electrochemical probe (such as ferrocene, ferricyanide) is provided upon binding analytes to the recognition elements decorating it. A progressively reduced redox activity of the probe is sensed by performing electrochemical measurements upon incubating increased concentrations of the analyte dispersed within the supporting matrix.

The above scheme has been largely used to determine cytokines levels using the immune-sensing approach (antigen-antibody recognition), also in biological fluids, by combining different electrode functionalization strategies and experimental measurement protocols [11,12]. The same scheme can be applied to other target molecules associated to inflammation states, including acute-phase proteins, serum amyloid A, fibrinogen, procalcitonin and calreticulin [13,14].

As regarding the cytokines, electrochemical electrode platforms (SPEs, IDEs) based on carbon materials have shown to be suitable for implementing electrodes coverage suited to a direct functionalization of their active surface. Sánchez-Tirado et al. have demonstrated multi-walled carbon nanotube (MWCNT)-modified SPEs with carbon WEs for the detection of TGF-beta 1, showing the biosensor suitability at working within the physiologic range in human serum of such cytokine [15]; Serafin et al. have decorated the carbon WE of SPEs by a MWCNTs/graphene quantum dots composite for the detection of Interleukin-13 receptor subunit alpha-2 down to the nanomolar range [16]. Within the above scenario, the work by Parate et al. indeed shows an interesting application of 3D printed graphene layers for the selective detection of cytokines in bovine minced implant supernatant as the biological matrix. They make use of a graphene-nanocellulose ink and an aerosol jet printer to implement well performing IDEs for interferon gamma (IFN-γ) and interleukin 10 (IL-10) detection [17].

Despite the demonstrated feasibility for efficient and selective biosensors targeted to cytokines detection, it emerges from literature that the proposed solutions often suffer from scarce indications concerning their reliability. In most cases, the reported calibration curves are nearly the outcome of measurements performed by using the *standard addition method*, where a single device is used for all the analyte concentrations under analysis, i.e. by measuring the biosensor response at analyte incubation steps defined by progressively increasing its concentration in the hosting biological matrix, within the desired concentration window to be investigated. This method is a standard laboratory practice that is important ~~by~~ from a fundamental basic research perspective. However, it may affect the device response due to possible fouling by proteins contained into the biomatrix on the electrode surface. Furthermore, it is limited in terms of applicability in real-life conditions, where an unknown concentration of analyte must be evaluated by recovering the device response. This is because the calibration curves assessed by the standard addition method depend on the individual response by the used electrode, whereas the device-to-device reproducibility currently is still affected by the SPEs fabrication methods and also needs for a proper control of both preparation (e.g. cleaning, as well as functionalization) and operation conditions [18].

Herein, we show the manufacturing and characterization of a SPE biosensor for the detection of IL-6 in saliva samples. The proposed SPE biosensor takes advantage from an organic layer made of a Thermal Exfoliated Graphene Oxide (TEGO) printed by the Aerosol Jet Printing (AJP) technique on its WE. Indeed, the defective surface of the TEGO layer allows a direct decoration of the WE by IL-6 antibodies (mAb IL-6) via carbodiimide chemistry, making it ready for the selective binding and recognition of IL-6. The TEGO layer provides a low cost and time-saving route to manufacture graphene-based WEs in SPEs biosensors, whereas commercial graphene inks provide defect free surfaces requiring post processing strategies aimed at inducing functional surface defects, such as oxygenated species, e.g. carboxyl and carbonyl groups, available for antibodies anchoring [17].

The TEGO layer was deposited on the WE by AJP, a technology extensively described in recent literature [19,20] and demonstrated to be well suited to 3D printed electronics [21] and bioelectronics [22]. Recently, AJP found applications oriented towards the healthcare, and its use in biosensing field is sustained by the rapid prototyping capability it offers, allowing to quickly fabricate large batches of devices aimed at pursuing a well reproducible response. Functional inks are formulated for the implementation of (bio)electronic devices as well [23]. AJP technique has been applied to fabricate biosensors for the electrochemical detection of proteins [24] and biomarkers [25], as well as to implement organic transistors for biosensing purposes [26,27]. At the state of our knowledge, this is the first time that a TEGO layer has been printed by AJP deposition.

Here we underline the importance of utilizing TEGO instead of gold as working electrodes for the biochemical functionality of the surface. TEGO deposited by AJP presents a highly defective exposed surface. While this is typically perceived as a drawback in terms of conductivity in the realm of graphene, in our case this disadvantage becomes a strength. In fact, the abundance of surface defects facilitates the attachment of antibodies on the underneath TEGO layer. This allows for the simultaneous achievement of two advantages in just one deposition step, i.e. (i) avoiding the functionalization of gold with thiols, thereby halving the total functionalization time, and (ii) increasing the free exposed surface area, thus enhancing sensor performance.

Taking into account the disposable nature of SPEs, we also designed a measurement protocol for the assessment of a reliable biosensor calibration curve from a *single shot measurement* [28,29,30]. It consists of Electrochemical Impedance Spectroscopy (EIS) measurements in presence of a redox probe carried out using a single electrode for each incubated IL-6 concentration spiked in a real saliva sample and falling within the desired interval (nominally, from 0.1 pg/mL to 10 ng/mL). A reference measurement, consisting of an EIS measurement performed without antigen incubation, is preformed prior to incubating the IL-6 spiked saliva and used to assess the device calibration curve.

Three calibration curves, expressed as the measured variations of the charge transfer resistance due to a red-ox probe at the WE prior and after IL-6 incubation, are extracted from data analysis.

Accordingly, the first calibration curve has been assessed by measuring six disposable devices for six IL-6 concentrations in the desired interval, hence using one device for each fixed concentration, and starting from the lowest concentration to the highest one. The second and third calibration curves are again determined using one device for each concentration, but randomly changing the measurement sequence of IL-6 concentrations within saliva samples, all this being made to mimic a real measurement where a given concentration produces similar responses by individual disposable devices. As a result, the as-determined calibration curves turn out to be quite similar each other, indicating that a high degree of control by the proposed functionalization protocol and satisfying device-to-device reproducibility are achieved. The scheme below (Fig. 1.A) reports the overall process of the experiment, where the fast preparation of the sensor, together with

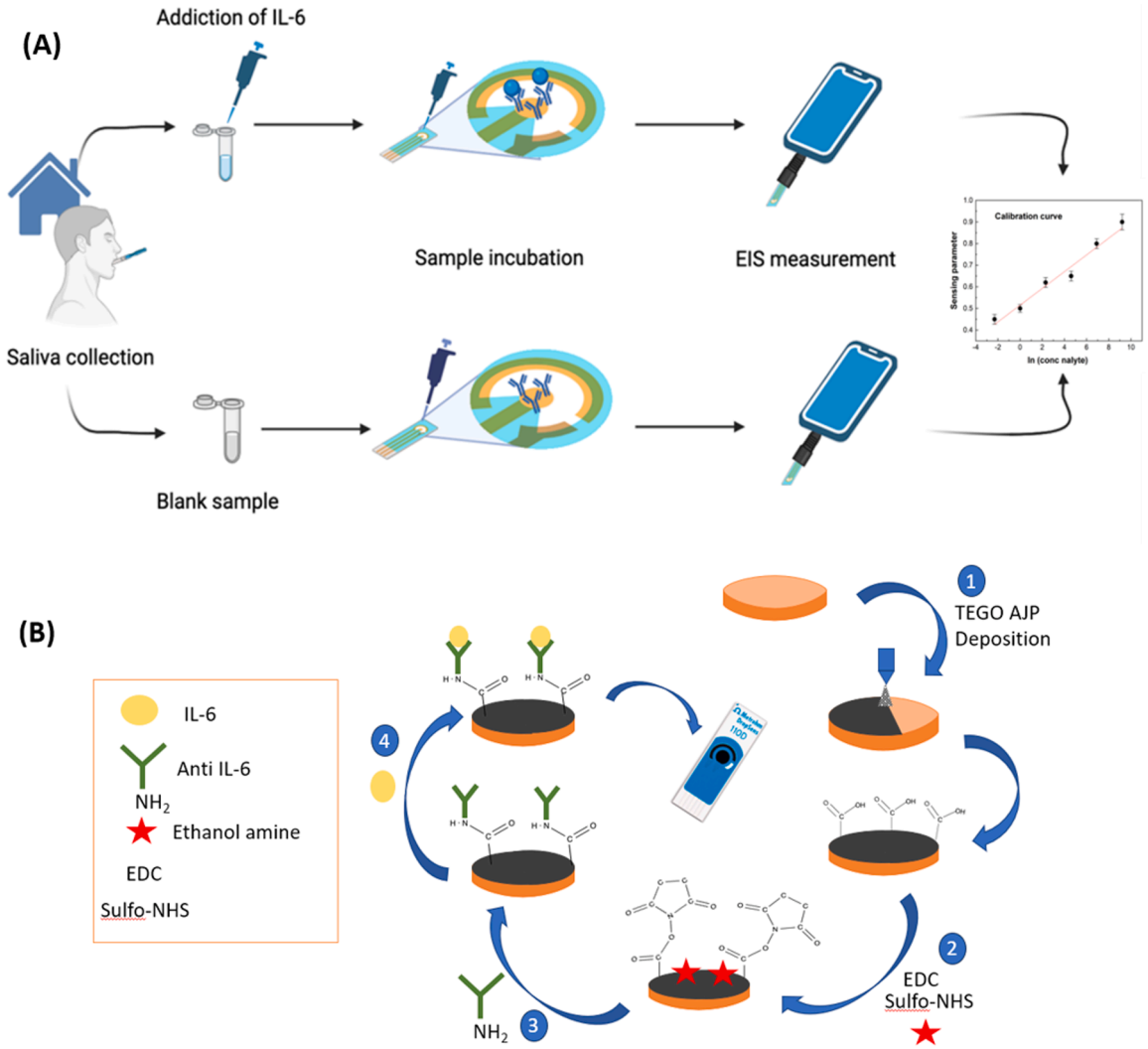

Fig. 1. (A) Scheme of the overall detection protocol starting from the saliva collection (upper panel, IL-6 spiked saliva; lower panel, blank), the easy incubation on the active sensor interface and the data collection/analysis.
(B) Scheme of the functionalization process: (1) TEGO deposition by AJP on Au WE; (2) activation of TEGO by EDC/NHS chemistry; (3) binding of antibodies (AntiIL-6) through their amine primary groups; (4) electrode ready for the incubation of biomatrices containing the reference IL-6 analyte (Created with BioRender).

saliva collection and device-to-device reproducibility make it suitable for usability even in domestic settings.

We want to emphasize the significance of our work, which represents a stride forward in basic research towards tangible and practical applications responding to the Affordable, Sensitive, Specific, User-friendly, Rapid/Robust, Equipment-free and Deliverable (ASSURED) criteria for Point of Care tests [31] provided by the World Health Organization (WHO). We have placed significant emphasis on the reproducibility of the sensor, particularly within an application-oriented perspective. This aspect is frequently overlooked in scientific literature, where the primary focus often lies in demonstrating proof of concept devices. This holds particularly true in the realm of biosensors, where calibration curves are typically constructed based on known concentrations. In our study, we aimed to devise a method that leverages the sensor's response along the calibration curve to discern concentrations previously unknown.

2. Experimental

2.1. Materials

Graphite powders (grade RW-A, average size 66 μm) were purchased from SGL Carbon. Sodium chlorate (ACS reagent, ≥99.0 %) was provided by Merck Co. Fuming nitric acid (99 %+), α-terpineol 1% wt, ethanolamine, bovine serum albumin (BSA), 1-ethyl-3-(3-dimethylaminopropyl)-carbodiimide (EDC), N-hydroxysulfosuccinimide sodium salt (sulfo-NHS), 2-(N-Morpholino) Ethane Sulphonic acid (MES) and fluoresceinamine isomer I were purchased from Sigma Aldrich Co. Cyclohexanone and methanol were acquired from Carlo Erba Reagents. IL-6 monoclonal antibodies have been purchased from Vinci Biochem Srl. From the electrochemical tests, SPEs from Metrohm Dropsens were considered using the 3-electrodes layout bearing the WE made of a 4 mm size Au disk, a Pt counter electrode (CE) and the Ag reference electrode (RE).

2.2. Synthesis of TEGO and ink preparation

The synthesis of Graphene Oxide by Thermal Exfoliation was carried out as follows. For the oxidation step, the Brodie method was employed: 5 g of graphite powder was ground in a mortar together with 40 g of sodium chlorate. The resulting powders were stirred and cooled in an ice bath, while 50 ml of fuming nitric acid was added stepwise. Then, the mixture was heated at 60 °C for 8 h. Subsequently, the mixture was diluted in Milli-Q water and filtered through a fritted Büchner funnel.

The solid fraction obtained was washed with a 1 M HCl solution to eliminate any residual salts, followed by thorough washing with Milli-Q water until the effluents reached a neutral pH. The resulting graphite oxide was then dried in an oven at 60 °C, ground into powder form and placed in a quartz tube under dynamic vacuum, which was quickly inserted in a tube furnace at 1150 °C and kept there for 30 min. This process resulted in the release of oxidized functional groups in the form of CO and CO_2, acting as propellants for the exfoliation and reduction of the graphene layers [32]. The TEGO powder has been used as the raw material for the preparation of a dedicated ink, suitable for printing by direct-writing techniques. The powder was mixed in cyclohexanone used as solvent (1 mg/mL); 5 mL of the resulting dispersion was ball-milled under a planetary ball milling (Fritsch Pulverisette). TEGO dispersion has been refined in zirconia jars with 24.5 g of 3 mm zirconia sphere at 650 rpm for a total time of 17.5 h (70 cycles for 15 min alternating from 1 min of pause in air). After milling, the dispersion achieves a water-like viscosity of ~ 7 cps, well suited for printing by the ultrasonic atomizer of the printer (AJP200, Optomec). To achieve a printable ink, a solution of TEGO dispersion 99% wt and α-terpineol 1% wt has been prepared. α-terpineol is a high boiling chemical that is expected to favor a decrease of the overspray effect during deposition process [33]. TEGO ink has been deposited using ultrasonic atomizer by loading 2 ml of the ink in the atomizer vial. Printing parameters for WE decoration are set to achieve the best compromise between overspray effect and line quality. In this respect, the TEGO printing pre-characterization (reported in Results and Discussion section) has shown that for a Focusing Ratio (FR) of 1 (carrier and sheath gases equal to 35 sccm) and for a platen temperature of 80 °C, a platen speed of 2 mm/*sec* allows meeting the requirement for high quality TEGO thin films deposition. The as-deposited graphene layers have been sintered at 220 °C for 30 min to remove α-terpineol residues prior to perform SEM micrographs (SEM-FIB Zeiss Auriga Compact) of the bare and covered SPE WEs. Before printing, the gold WE was subjected to a deep cleaning process consisting of three consecutive brushings in methanol, followed by 20 Cyclic Voltammetry (CV) cycles (in the range from −0.8 to 1.2 V) by a Palmsens4 potentiostat (also used for biosensors electrochemical characterization) in sulfuric acid (H_2SO_4, 0.1 M).

3. Electrode functionalization and measurement protocol

The surface of the printed TEGO has been chemically activated for binding the anti-IL6 antibodies. Fig. 1.B reports the scheme of the overall biofunctionalization process after TEGO decoration (Fig. 1.B (1)). A solution of 100 mM of sulfo-NHS mixed in 10 mM of MES buffer at pH=5.5 is used for the activation of carboxylic groups (COOH) of the printed TEGO layer (Fig. 1.B (2)). A drop of 60 μL is casted over the WE electrode and left soaking for 1 h lasting incubation inside a customized incubation chamber, made of a water salt bath to slow down the solvent evaporation. After the incubation, a cleaning step in PBS is applied. A fluorescence molecule is incubated at this time on some test samples to verify the effective activation of carboxyl groups of the TEGO surface: a 0.5 mg/mL of fluoresceine-ammine dissolved in PBS is incubated over the electrode surface for 2 h. After activation, the TEGO surface was treated with the anti-IL-6 molecule to induce its effective binding with the activated carboxylic groups (Fig. 1.B (3)); to this aim, we have tested different mAb IL-6 concentrations in PBS, and 50 μL of a PBS solution with 0.2 μm/μL of the antibody incubated for 2 h on the WE has been found to be the best decoration protocol for effective IL-6 detection. As the final step of the biofunctionalization protocol, the free sites residues have been passivated by incubation with 100 mM of ethanolammine followed by incubation with 1% w/v BSA (Bovine Serum Albumin) in PBS buffer for 30 min. The surface is now ready for the incubation of the IL-6 molecule (duration, 1 h) (Fig. 1.B (4)). The total time of the whole process was 4 h. IL-6 incubation was carried out in saliva as collected by dedicated saliva samples collectors (Salimetrics, LLC) and following indications provided in ref [34]. The as-collected saliva samples were transferred in a 15 ml sterile tube, and then centrifuged at 3000 rpm x 10′, for cells and debris removal. To obtain a dose-response curve, recombinant IL-6 was diluted in freshly saliva at various concentrations within the concentration interval comprising the dynamic range of an ELISA assay, i.e. from 0.1 pg/ml to 10 ng/ml; in this way, we built a library of 6 saliva samples with different IL-6 spikes.

For measurements, 50 μl of samples were incubated on the WE for 1 h and then EIS was performed as described in the previous paragraph. The dynamics of IL-6 binding has been preliminary checked by EIS measurements (see section S.1, Supplementary Information file). Each concentration was accordingly used with a dedicated TEGO-functionalized SPE, hence wasted after the assessment of the sensor response prior and after incubating the related saliva sample.

The collected saliva sample has been preliminary tested by an ELISA assay using the Ella-SimplePlex system (Bio-Techne, Minneapolis, MN, USA). The experiment was conducted as per manufacturer instructions. Briefly, saliva samples were freshly collected and centrifuged at 5000 rpm for 5 min and then diluted with sample diluent buffer, as indicated by manufacturer instructions.

A basal value of IL-6 content equal to 0.4 pg/ml has been found.

4. Surface characterization

Micro-Raman spectroscopy was conducted using a Horiba Jobin Yvon LabRam micro-spectrometer (HORIBA Scientific, Kyoto, Japan), employing a double Nd:YAG laser with a 473.1 nm as excitation line, an Olympus BX40 microscope (Olympus, Tokyo, Japan), through a ULWD 50x objective, and a Peltier-cooled silicon CCD. The spectral range from ~1000 to 2000 cm^{-1} was considered to encompass the D and G Raman bands of the graphene-based material. Calibration of the instrument was conducted using the Raman signal of standard silicon reference at 520.6 cm^{-1}. The spectral resolution was 4 cm^{-1}. Density filters were used to reduce the laser beam power and prevent excessive heating of the carbon-based samples. The standard analysis involved acquiring 10 consecutive accumulations, each lasting 60 s. XPS spectra have been acquired in an Ultra-High-Vacuum (UHV) system using a VSW HA100 hemispherical electron energy analyzer with PSP power supply/control and a non-monochromatized Mg Kα source (photon at 1253.6 eV), with a final energy resolution of 0.86 eV. The binding energy (BE) scale was calibrated from the Au4f 7/2 peak at 84.0 eV of a sputtered Au surface. The core level analysis was performed by Voigt lineshape deconvolution after the background subtraction using a Shirley function. The typical precision for each component's energy position is ±0.05 eV. The uncertainty for the full width at half-maximum (FWHM) is less than ±2.5 %, while it is about ±2 % for the area evaluation. The analysis has been carried out on printed TEGO films made of one and two layers. Fluorescence microscopy has been used to test the functionalization efficiency. To this aim, a 0.5 mg/mL solution of fluorescein amine in methanol is incubated over the electrode surface for 2 h. Fluorescence analysis has been conducted positioning a PBS drop over functionalized WE and covered by a microscope glass slide, using a Nikon Eclipse Ni-E microscope (FITC filter, magnification 10X).

4.1. Biosensors response characterization

The biosensors' response was assessed by EIS measurements performed before and after each IL-6 binding process and using a ferrocene solution as the electrochemical probe (5 mM in PBS 0.1 M). In particular, ferrocene realizes a reversible one-electron red-ox process to perform Fe^{2+}/Fe^{3+} change at gold electrodes (half-wave potential from CV measurements of about 0.3 mV vs. SCE [35]). Nyquist plots (as discussed in the next section) have been accordingly acquired by applying a small amplitude (E_{ac}=10 mV) sinusoidal signal with frequency ranging between 0.1 Hz and 100 KHz. Charge transfer resistance values, R_{ch}, may be extracted from the Nyquist plots by analyzing equivalent model circuits and used to define the biosensor's sensing parameter.

To assess the reproducibility of the measurements, for each electrode a reference EIS measurement on SPEs WEs coated by TEGO decorated with mAb IL-6 was acquired, i.e. prior to carrying out the antigen incubation. Reference measurements, providing a charge transfer resistance denoted as $R_{ch,0}$, are used for normalizing the sensor response acquired at a given antigen concentration. In this way, a relative change of the charge transfer resistance, ΔR_{ch}, assessed by measuring R_{ch} prior ($R_{ch,0}$) and after ($R_{ch,1}$) the antigen incubation, may be set as the sensing parameter ($\Delta R_{ch} = (R_{ch,1}-R_{ch,0}) / R_{ch,0}$)). Providing that a good control of the electrodes decoration by antibodies may be accomplished through practice, relative variations of the as-defined sensing parameter are waited to reduce the variability on the sensing response eventually induced by reproducibility issues [18]. Biosensor's blank response (i.e. biosensor response acquired in presence of blank saliva samples, without IL-6 aliquots, and scaled by the above defined reference measurements) have also been recorded to assess the sensor's Limit of

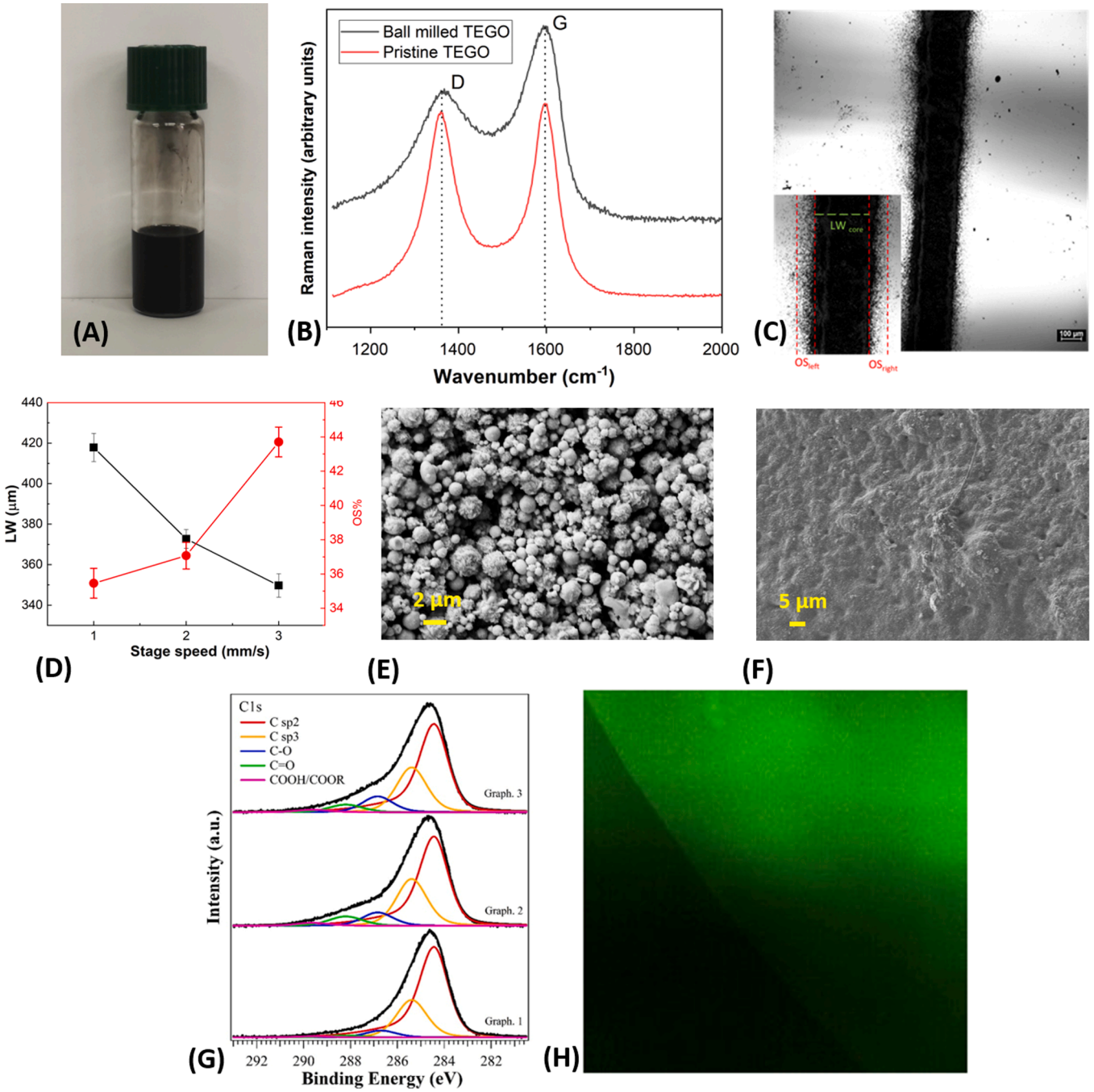

Fig. 2. A) TEGO dispersion after 17.5 h ball-milling in Cyclohexanone; B) Raman spectra for pristine and ball-milled TEGO powders; C) Optical image of TEGO printed lines at FR=1 and stage speed $v = 2$ mm/sec (in the inset, a magnification of printed line with definition of overspray region and line core); D) Representation of the line core width (LW) and overspray percentage (OS%) trends as a function of v. Each point is the mean of five identical printed lines (error bars are calculated as the error the standard error of the mean from LWs assessed from three homologue TEGO lines); SEM images of the screen printed Au working electrode (E) before TEGO deposition (SEM parameters ETH=20 KV, WD=10 mm, Magnitude= 10 K) and (F) after TEGO deposition (SEM parameters ETH=5 KV, WD=9.8 mm, Magnitude= 2 K); G) XPS analysis of C1s core level for three films at increasing coverages (from one to three TEGO layers). Spectra are background subtracted and normalized in height; H) Fluorescence image of the TEGO surface functionalized with fluoresceinamine. The molecule was deposited as a drop on the activated surfaces and it is clearly distinguishable the edge of the drop.

Detection (LoD) from calibration curves and blank measurements. The electrodes were systematically cleaned in PBS immediately after each blank measurement to reduce fouling of saliva proteins on their surface.

5. Results and discussion

Fig. 2.A shows the TEGO ink dispersion obtained after milling. The dispersion appeared homogeneous and with a long stability time (more than 1 month) before the appearance of agglomerates. Chemical characterization of TEGO powder is achieved via Raman spectroscopy. Results from Raman analysis are reported in Fig. 2.B, where a comparison between Raman spectra of pristine and ball-milled TEGO powders is shown. As typically observed in carbon-based materials, the Raman spectra exhibit two broad bands at ~1350 cm^{-1} and ~1600 cm^{-1}, respectively. These signals are related to the D and G bands: the former is ascribed to structural defects and disorder while the latter is referred to the E_{2g} vibrational mode of the sp^2 graphitic domains [36]. In our case, an increase in the widening of the D band is observed in the ball-milled sample as compared to the TEGO precursor, indicating an enhancement of the in-plane defectivity, i.e. an increase of oxidized moieties and a structural disorder (e.g. sp3 carbon, amorphous regions) as a consequence of the ball-milling process.

Ink characterization was carried out to define the printing parameters to achieve the best compromise between overspray (OS) effect and line quality (OS being the indication of defects at the line edges). This is done by varying the platen speed (v) and measuring the total line width (LW) and percentage of overspray (OS%) for each speed, keeping both the nozzle diameter and the Focusing Ratio (FR) constant. FR and the nozzle size are kept constant to simplify the characterization process, where only *v* acts as a variable parameter. In this way, it is possible to investigate how *v* affects the OS phenomenon [22,37] and overwetting effects due to use of a low volatile solvent (such as cyclohexanone). Accordingly, TEGO lines were deposited by varying *v* from 1 to 5 mm/*sec*, and 5 lines were printed for each v. FR was set to 1 (carrier and sheath gases equal to 35 and 35 sccm, respectively), while the platen temperature was fixed at 80 °C. Before deposition, 5 min of stabilization time were waited to avoid drifting and instability of ink during the printing process.

An optical micrograph of a printed line is shown in Fig. 2C, while Fig. 2D shows the trend of LW and OS% as a function of v. In agreement with literature [38], LW decreases upon increasing v, while OS% is lowered for increasing speeds. Since the best compromise is obtained for $v = 2$, this value was adopted as the process speed for WE decoration by TEGO. Stage speed values of 4 and 5 mm/*sec* (not reported in Fig. 2D) are too high for our customized ink, as the deposited lines are discontinuous and their quality is highly dependent on the substrate features (defects, poor wettability). The selected printing parameters for Au WE decoration by TEGO layers are reported in Table 1.

SEM micrograph of bare SPE WEs reported in Fig. 2.E shows that the highly rough surface commercial electrodes is completely dominated by a granular morphology [18]. While large-sized flakes and sheets are waited upon thermal exfoliation [39,40], the smooth morphology of TEGO decorating surface, indicated by the SEM micrograph of Fig. 2.F, may act as a supporting factor towards the pursuit of an enhanced device-to-device reproducibility. Surface smoothness can be ascribed to the ball milling process, whose effect is to assist an increase of defectivity while reducing, at the same time, the sheets' size down to a length scale compatible with AJP deposition systems [19].

Table 1
Selected printing parameters for the decoration of gold WEs by TEGO.

Ink	Nozzle (μm)	SH (SCCM)	CH (SCCM)	Platen temperature (°C)	Platen speed (mm/s)	Current (mA)
TEGO	200	35	35	80	2	0,5

The chemical characterization of the deposited TEGO layers was achieved via XPS analysis (Fig. 2.G). In this specific case, we performed XPS analysis to deeply evaluate the surface chemistry of three samples differing each other for the number of printed TEGO layers (from one to three). The analysis revealed the presence of carbon (72.3–74.3 % of the total signal, in atomic percentage), oxygen (15.0–18.3 %) and other minor species (in particular Zr and Si, mainly related to the mechanical treatments). In detail, C1s core level for the three samples shows several components located at the same BEs but with slightly different intensities. The main peak is located at 284.44 eV and related to the sp^2 carbon atoms in graphene, showing an asymmetry due to the presence of few graphene layers [41]. The long tail at higher BEs reveals the presence of either sp^3 carbon (peak at 285.39 eV), typically related to defects in the layered structure [42], and oxidized carbon, namely C—O (~286.75 eV), C = O (~288.2 eV) and COOH/COOR (~289.6 eV) [43]. The weights of the oxidized components on the C1s signal undergo variations from low to higher coverages, achieving a maximum in the second sample (denoted as *Graph.2* in Fig. 2.G). For this reason, the IL-6 detection has been carried out using WEs covered by depositing two TEGO layers. The biochemical functionalization of the printed TEGO layers (sketched in Fig. 1.B) is performed by sequential steps, following a protocol based on the EDC/NHS activation reaction chemistry [44]. The process of TEGO biochemical functionalization results quite shorter in time with respect to gold-thiolation approaches, and does not require other post deposition treatments, such as for instance chemical modifications by pyrene-chemistry [45]. The decoration process by selected antibodies can be completed within one day, while four days may be required for functionalizing bare gold WEs and two days for other graphene-type electrodes. The printed TEGO does not require any chemical modification before carrying out the biochemical functionalization, thanks to the high density of defects and oxidized moieties on its surface, as shown by XPS characterization. These peculiar chemical properties make the TEGO particularly suitable for antibody anchoring and, therefore, for antigen detection. Fig. 2.H reports the fluorescein signal after immobilization on EDC/NHS activated TEGO layer as a drop, confirming the molecule binding. EIS probes the total impedance ($Z = Z' + iZ''$, where Z' and Z'' are the real and imaginary parts of the total impedance, Z) at the WE as a function of the ac frequency of a small amplitude (mV range) sinusoidal signal. The Nyquist plot is a complex plane representation of EIS data, where Z'' is plotted as a function of Z'. It provides information about charge and/or mass transfer and on diffusion processes via a modeling performed by equivalent circuits analysis [46]. EIS is also used to evaluate the suitability of the functionalization protocol. Fig. 3.A shows the Nyquist plots for gold WEs covered by untreated TEGO, after its treatment with EDC—NHS (activation of oxygenated groups) and after anti IL-6 binding at the activated surface sites. Aimed at assessing the sensing parameter to build up a calibration curve for the IL-6 biosensor, collected EIS data were fitted by using a Randles circuit comprising the charge transfer resistance (R_{ch}), a constant phase element (CPE) and a Warburg (W) element (see the inset of Fig. 3.B). The charge transfer resistance $R_{ch,1}$ extracted for each incubated concentration is the informational parameter, and its relative variation (ΔR_{ch}) with respect to its value calculated without incubation ($R_{ch,0}$, i.e. R_{ch} assessed from reference measurements) is used as the figure of merit of the electrochemical biosensor. The enhancement of R_{ch} - as a result of the enlargement of the semicircles in Nyquist plots occurring in the low (Z',Z'') region- indicates that the charge transfer efficiency suffers from properly accomplished functionalization steps [47]. Our main effort was focused on device-reproducibility in presence of biological samples, in order to make a step forward to real applications. Each experimental point over the calibration curve is determined by measuring the SPE response for pre- and post-incubated WEs, all this using three different devices for each IL-6 nominal concentration and averaging the related responses. Overall, the calibration curve is the outcome of a total of 18 measurements and 18 different devices, probing the efficiency of TEGO layer in providing a device-to-device

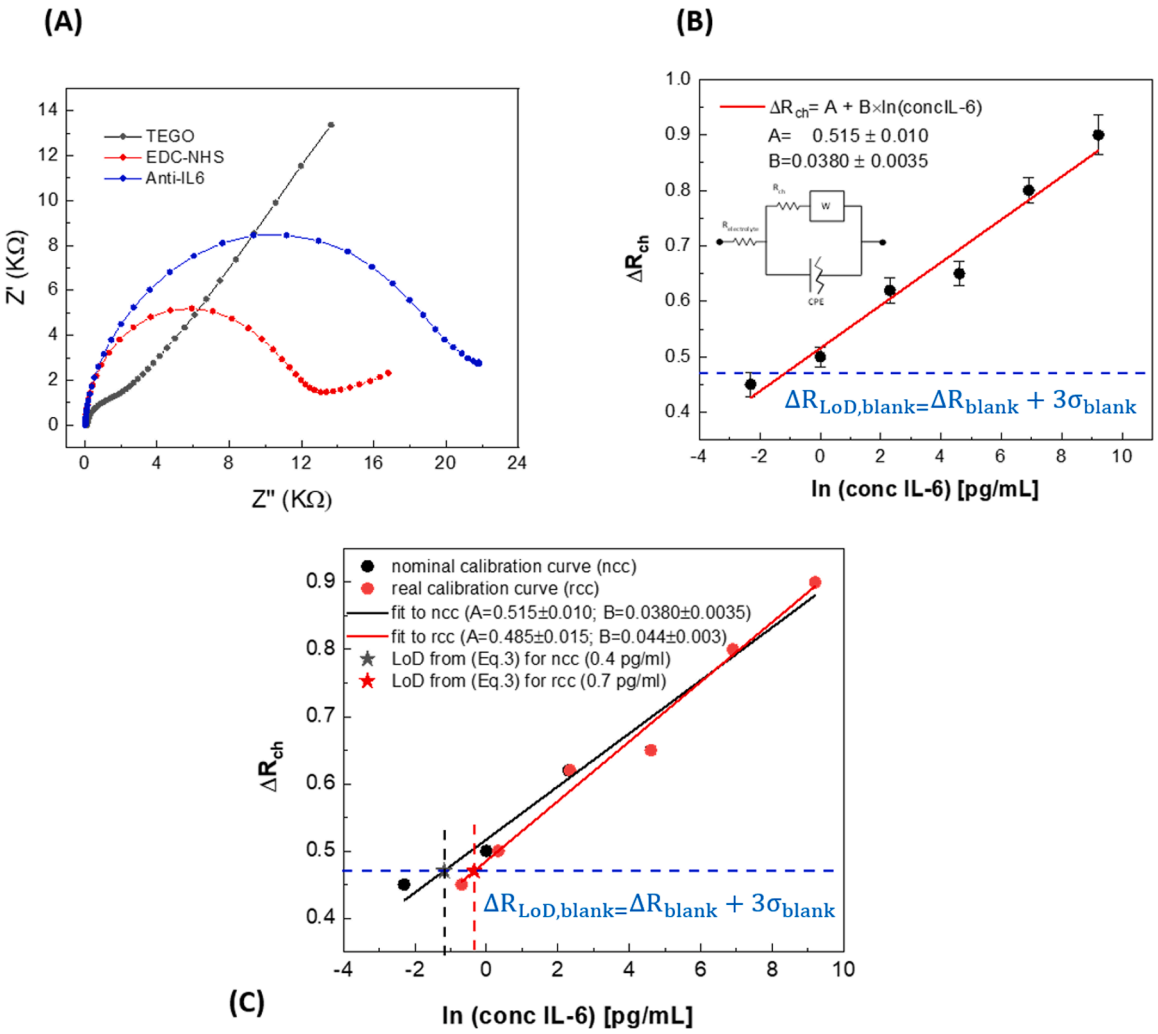

Fig. 3. (A) Nyquist plots for untreated TEGO (black line-symbols), after its treatment with EDC—NHS (red line-symbols) and after anti IL-6 binding at the activated surface sites (blue line-symbols); (B) overall calibration curve of the IL-6 biosensor in real saliva samples. The curve is determined from a total of 18 devices. In this respect, each reported point is the average of 3 independent measurements; error bars are calculated as the standard error of the mean (the red dashed line represents the linear regression in the lin-ln plot; the Randles circuit is also reported as figure inset); (C) calibration curves for nominal (black circles) and real (red circles) IL-6 concentrations in saliva samples. Black and red lines are the related fitting curves to the calibration plot (ΔRch=A+Bln(concIL-6)), while black and red star symbols represent the $\left(\frac{\Delta R_{LoD,blank}-A}{B}\right)$ factor of Eq. 3 for nominal and real calibration concentrations.

reproducibility. Fig. 3.B shows the calibration curve of the sensor, representing the overall normalized sensor response as a function of the IL-6 concentration. Small error bars, calculated as the standard error of the mean (i.e. $\sigma/\sqrt{N}$, where σ is the standard deviation from the average on N measured events), indicate low uncertainty/high reproducibility upon measuring different electrodes at a given analyte concentration.

As reported by many literature works [48,49,50], the curve shows a linear dependence in the lin-log plot, hence the sensor dynamic range covers the concentration range where inflammation states may occur. Analytical methods allow LoD evaluation from the calibration curves, as well as from blank measurements, following different literature approaches. Assuming a Gaussian distribution for the assessed blank measurements, a common method to define the LoD from the calibration curve makes use of the equation $LoD = \frac{3\sigma_{blank}}{B}$, where σ_{blank} is the standard deviation calculated from the blank distribution, B is the slope of the (linear) sensor calibration curve ($y = A+Bx$) and the numerical factor 3 determines a confidence level of 95 %, i.e. less than 5 % of the assessed LoD values fall within the blank signal distribution. Although also used in the case of calibration curves showing a logarithmic behavior [48,51], this approach is actually incorrect because it may be applied only when the calibration curve is linear and for intervals of low analyte concentrations (i.e. where the sensor response is slightly higher than the blank signal[52]). In our case, it may be provided a LoD concentration value from the equation:

$$LoD = 3\sigma^{blank}_{(conc-IL6)}, \tag{1}$$

where $\sigma^{blank}_{(conc-IL6)}$, the standard deviation of the analyte concentration at the blank level, is calculated taking into account the logarithmic behavior of the sensor response ($\Delta R_{ch}=A + B\cdot\ln(concIL\text{-}6)$) as [49]:

$$\begin{aligned}\sigma^{blank}_{(conc-IL6)} &= \left(\frac{\partial conc - IL6}{\partial \Delta R_{ch}}\bigg|_{\Delta R_{blank}}\right)^2 \times \sigma^2_{blank} + \left(\frac{\partial conc - IL6}{\partial A}\right)^2 \times \sigma^2_A \\ &\quad + \left(\frac{\partial conc - IL6}{\partial B}\right)^2 \times \sigma^2_B \\ &= \frac{exp\left(\frac{\Delta R_{blank}-A}{B}\right)}{B}\left[\sigma^2_{blank} + \sigma^2_A + \left(\frac{\Delta R_{blank}-A}{B}\right)^2 \sigma^2_B\right]^{\frac{1}{2}}.\end{aligned} \tag{2}$$

Here, we recall that $\Delta R_{blank}=(R_{blank}-R_{ch,0})/R_{ch,0}$ is the sensing parameter at the blank level and σ_{blank} is the related standard deviation, while A and B are extracted by a fitting procedure and $\sigma_{A,B}$ are the

standard deviations of such parameters (fitting parameters A, B, σ_A and $\sigma_{A,B}$ used for LoD calculation are reported in Fig. 3.B). Considering that the device response for blank measurements (no IL-6 spiked saliva) provides a mean value for the sensing parameter $\Delta R_{blank} = 0.2$ with $\sigma_{blank} = 0.09$, a LoD of 1×10^{-2} pg/ml is calculated using Eq. 2. Worth to note that ΔR_{blank} has been assessed for a real concentration of 0.4 pg/ml (blank basal IL-6 level of collected saliva, as measured by the ELISA assay), hence the lowest nominal concentration values of 0.1 and 1 pg/ml would correspond to real values of 0.5 and 1.4 pg/ml. Actually, such concentrations are still well within the normal IL-6 levels [3] and the contribution of the basal blank level becomes increasingly negligible for higher IL-6 concentrations spiked in collected saliva. Although it is suggested to calculate a LoD in the low concentration limit where spike in analyte levels do not exceed the expected LoD more than a factor ten, the assessed calibration curve is indicative of a sensor effective in properly detecting IL-6 for concentrations compatible with cytokine storm occurrence. Indeed, considering the actual concentration values, the related 'real' calibration curve slightly deviates from the 'nominal' one reported in Fig. 3.B and compared with the former in Fig. 3.C. The LoD value of 1.7×10^{-2} pg/ml assessed from Eq. 2 in the case of the real calibration curve slightly deviates from that from nominal calibration curve, still confirming the biosensor effectiveness for severe inflammation diagnosis.

The biosensor's LoD may also be assessed from blanks (collected saliva without addition of IL-6 aliquots) considering the mean value of all the acquired blank measurements, ΔR_{blank}, and imposing that less than 5 % of the measured charge transfer resistance of such blanks falls within the region of false negatives. This may be done defining the LoD for the sensor parameter as $\Delta R_{LoD,blank} = \Delta R_{blank} + 3\sigma_{blank}$ (Fig. 3.B, $\Delta R_{LoD,blank} = 0.47$, blue dashed line). To translate it in terms of analyte concentration, a LoD_{conc}^{blank} value may be assessed from the regression curve and related parameters reported in Fig. 3.B and C, as:

$$LoD_{conc}^{blank} = exp\left(\frac{\Delta R_{LoD,blank} - A}{B}\right), \quad (3)$$

From (Eq. 3) LoD_{conc}^{blank} values of 0.3 and 0.7 pg/ml are assessed from fitting parameters extracted from nominal and real calibration curves, respectively. Both the assessed LoD_{conc}^{blank} values are 1 order of magnitude higher than the LoD values calculated from (Eq. 2) but, in any case, still comparable with the concentration of 0.4 pg/ml showed by the actual blank saliva sample (i.e. the collected one). This means that the basal IL-6 level of the collected saliva sample does not induce any significant change of the sensor response into the analyzed concentrations window. In any case, it is to be outlined that the discrepancy between the assessed LoD values indicates that LoD evaluation is strongly dependent on the implemented experimental methods and modelling approaches. In our case, the first method is confirmed to provide a lower LoD value as it also takes into account the variance on the intercept of the regression curve [49].

Finally, a comparison between the proposed SPE biosensors and standard ELISA assay for salivary IL-6 detection, discussed in section S.2 of the Supplementary Information file, has indicated that the responses of our biosensor and ELISA assay well correlate with each other.

Although our approach demonstrates the potential of SPEs biosensors to provide a reproducible calibration response for IL-6 immunosensors in real saliva samples, currently the sole determination of IL-6 levels yields poor information about an overall health state. More interesting is looking for a "signature" given by a set of molecular targets, such as TFA, IL-6 and IL-13, whose correlation may give much more information. Multiple detection routes based on the use of SPEs' array to reliably identify the risk of an ongoing cytokine storm in case of different diseases, are in progress.

6. Conclusions

SPE immunosensors based on time- and cost-consuming standard methods of fabrication are often subjected to a low device-to-device reproducibility, also due to a variability of WEs morphology that influences the formation of antibody SAM layers for antigen recognition.

Measurement protocols used in lab practice and widely reported in literature are mostly based on the *standard addition methods*, which are merely suitable to test "on bench" the potential of biosensors upon assessing a calibration curve using a single device. In this work, we proposed an alternative method of antibody functionalization of SPEs' WE, consisting of their modification by deposition of defective carbon-based layers (i.e. TEGO) using a rapid prototyping approach (i.e. AJP technique). The defectivity of TEGO layers has demonstrated to implement time saving protocols for electrodes biofunctionalization that, in combination with the proposed method for sensor characterization/data analysis, opens a route for application in relevant environment by low-cost devices. Accordingly, in this work we have implemented SPE biosensors for the detection of IL-6 in real saliva samples via analysis of EIS response. The final calibration curve has been assessed as the mean of three independent experiments performed using individual devices for each concentration and scaling the SPEs' EIS response with respect to reference measurements, i.e. EIS analyses on antiIL-6 functionalized WEs without any antigen incubation. In this way, a small variability among assessed calibration curves has been found. The proposed biosensor is effective in detecting IL-6 in spiked saliva samples for concentrations falling within the range of interest for diagnostics of cytokine storm, showing a lowest limit of detection of 1×10^{-2} pg/ml, demonstrating superior performance in terms of sensitivity, specificity, and detection limits with respect to printed biosensors reported in literature. Our approach points the way for the development of rapid and reliable biosensors that meet the demand for high sensitivity and repeatability in biomarkers detection in freshly collected saliva samples.

Disclaimer

Funded by the European Union. However, the views and opinions expressed are hose of the authors alone and do not necessarily reflect those of the European Union or the European Commission. Neither the European Union nor the European Commission can be held responsible for them.

Ethical aspect

The collection of saliva was performed at the Department of Precision Medicine "Luigi Vanvitelli" from a healthy volunteer. All methods were carried out in accordance with the Declaration of Helsinki. The healthy participant to the study gave informed consent.

CRediT authorship contribution statement

D. Vurro: Conceptualization, Writing – original draft, Investigation, Visualization. **L. Pasquardini:** Conceptualization, Validation. **M. Borriello:** Conceptualization, Investigation. **R. Foresti:** Investigation, Validation. **M. Barra:** Conceptualization, Validation. **M. Sidoli:** Investigation. **D. Pontiroli:** Investigation. **L. Fornasini:** Investigation. **L. Aversa:** Investigation. **R. Verucchi:** Investigation. **P. D'Angelo:** Conceptualization, Writing – original draft, Visualization, Supervision. **G. Tarabella:** Conceptualization, Writing – original draft, Supervision.

Declaration of competing interest

The authors declare that they have no known competing financial interests or personal relationships that could have appeared to influence the work reported in this paper.

Data availability

Data will be made available on request.

Acknowledgements

The research presented herein has been partially supported by the SMARTPROSYS project (n. 2022T5MN35) under the PRIN progetti di ricerca di rilevante interesse nazionale—Bando 2022, MUR, Italy

D.V., P.D. and G.T. have been supported by the project "RAISE – Robotics and AI for Socio–economic Empowerment" under the European Union – NextGenerationEU.

G.T and P.D gratefully acknowledge the support from the European Union's Horizon Europe research and innovation program under the Pathfinder Challenge grant agreement No. 101115545 — IVLab.

M. Borriello acknowledges Regione Campania for supporting her within the "Avviso Pubblico per l'acquisizione di manifestazioni di interesse per la realizzazione di servizi di ricerca e sviluppo per la lotta contro il Covid-19" – DD n° 150.

We wish to thank Dr. Aris Liboà for technical support.

Supplementary materials

Supplementary material associated with this article can be found, in the online version, at doi:10.1016/j.snr.2024.100211.

References

[1] M. Rincon, Interleukin-6: from an inflammatory marker to a target for inflammatory diseases, Trend. Immunol. 33 (2012) 571–577, https://doi.org/10.1016/j.it.2012.07.003.
[2] C. Rolhion, F. Penault-Llorca, J.-L. Kémény, J.-J. Lemaire, C. Jullin, C. Labit-Bouvier, F. Finat-Duclos, P. Verrelle, Interleukin-6 overexpression as a marker of malignancy in human gliomas, J. Neurosurg. 94 (2001) 97–101, https://doi.org/10.3171/jns.2001.94.1.0097.
[3] A. Aleksandra Nielsen, J. Nederby Nielsen, A. Schmedes, I. Brandslund, H. Hey, Saliva Interleukin-6 in patients with inflammatory bowel disease, Scand. J. Gastroenterol. 40 (2005) 1444–1448, https://doi.org/10.1080/00365520510023774.
[4] B. Hu, S. Huang, L. Yin, The cytokine storm and COVID-19, J. Med. Virol. 93 (2021) 250–256, https://doi.org/10.1002/jmv.26232.
[5] K. Guo, S. Wustoni, A. Koklu, E. Díaz-Galicia, M. Moser, A. Hama, A.A. Alqahtani, A.N. Ahmad, F.S. Alhamlan, M. Shuaib, A. Pain, I. McCulloch, S.T. Arold, R. Grünberg, S. Inal, Rapid single-molecule detection of COVID-19 and MERS antigens via nanobody-functionalized organic electrochemical transistors, Nat. Biomed. Eng. 5 (2021) 666–677, https://doi.org/10.1038/s41551-021-00734-9.
[6] L. Fabiani, M. Saroglia, G. Galatà, R. De Santis, S. Fillo, V. Luca, G. Faggioni, N. D'Amore, E. Regalbuto, P. Salvatori, G. Terova, D. Moscone, F. Lista, F. Arduini, Magnetic beads combined with carbon black-based screen-printed electrodes for COVID-19: a reliable and miniaturized electrochemical immunosensor for SARS-CoV-2 detection in saliva, Biosens. Bioelectron. 171 (2021) 112686, https://doi.org/10.1016/j.bios.2020.112686.
[7] M. Thanihaichelvan, S.N. Surendran, T. Kumanan, U. Sutharsini, P. Ravirajan, R. Valluvan, T. Tharsika, Selective and electronic detection of COVID-19 (Coronavirus) using carbon nanotube field effect transistor-based biosensor: a proof-of-concept study, Mater. Today Proc. 49 (2021) 2546–2549, https://doi.org/10.1016/j.matpr.2021.05.011.
[8] K.G. Gunasinghe Pattiya Arachchillage, S. Chandra, A. Williams, S. Rangan, P. Piscitelli, L. Florence, S. Ghosal Gupta, J.M. Artes Vivancos, A single-molecule RNA electrical biosensor for COVID-19, Biosens. Bioelectron. 239 (2023) 115624, https://doi.org/10.1016/j.bios.2023.115624.
[9] M. Song, X. Lin, Z. Peng, S. Xu, L. Jin, X. Zheng, H. Luo, Materials and methods of biosensor interfaces with stability, Front. Mater. 7 (2021), https://doi.org/10.3389/fmats.2020.583739.
[10] N.L. Walker, A.B. Roshkolaeva, A.I. Chapoval, J.E. Dick, Recent advances in potentiometric biosensing, Curr. Opin. Electrochem 28 (2021) 100735, https://doi.org/10.1016/j.coelec.2021.100735.
[11] M. de L. Gonçalves, L.A.N. Truta, M.G.F. Sales, F.T.C. Moreira, Electrochemical point-of care (PoC) determination of interleukin-6 (IL-6) using a pyrrole (Py) molecularly imprinted polymer (MIP) on a carbon-screen printed electrode (C-SPE), Anal. Lett. 54 (2021) 2611–2623, https://doi.org/10.1080/00032719.2021.1879108.
[12] D.J. Pérez, E.B. Patiño, J. Orozco, Electrochemical nanobiosensors as point-of-care testing solution to cytokines measurement limitations, Electroanalysis 34 (2022) 184–211, https://doi.org/10.1002/elan.202100237.
[13] A. Menzel, H. Samouda, F. Dohet, S. Loap, M.S. Ellulu, T. Bohn, Common and novel markers for measuring inflammation and oxidative stress ex vivo in research and clinical practice— Which to use regarding disease outcomes? Antioxidants 10 (2021) 1–61, https://doi.org/10.3390/antiox10030414.
[14] E.B. Aydln, M. Aydln, M.K. Sezgintürk, Impedimetric detection of calreticulin by a disposable immunosensor modified with a single-walled carbon nanotube-conducting polymer nanocomposite, ACS Biomater. Sci. Eng. 8 (2022) 3773–3784, https://doi.org/10.1021/acsbiomaterials.2c00499.
[15] E. Sánchez-Tirado, A. González-Cortés, P. Yáñez-Sedeño, J.M. Pingarrón, Carbon nanotubes functionalized by click chemistry as scaffolds for the preparation of electrochemical immunosensors. Application to the determination of TGF-beta 1 cytokine, Analyst 141 (2016) 5730–5737, https://doi.org/10.1039/C6AN00941G.
[16] V. Serafín, A. Valverde, G. Martínez-García, E. Martínez-Periñán, F. Comba, M. Garranzo-Asensio, R. Barderas, P. Yáñez-Sedeño, S. Campuzano, J. M. Pingarrón, Graphene quantum dots-functionalized multi-walled carbon nanotubes as nanocarriers in electrochemical immunosensing. Determination of IL-13 receptor α2 in colorectal cells and tumor tissues with different metastatic potential, Sens. Actuat. B Chem. 284 (2019) 711–722, https://doi.org/10.1016/j.snb.2019.01.012.
[17] K. Parate, S.V. Rangnekar, D. Jing, D.L. Mendivelso-Perez, S. Ding, E.B. Secor, E. A. Smith, J.M. Hostetter, M.C. Hersam, J.C. Claussen, Aerosol-Jet-Printed Graphene Immunosensor for Label-Free Cytokine Monitoring in Serum, ACS Appl. Mater. Interface. 12 (2020) 8592–8603, https://doi.org/10.1021/acsami.9b22183.
[18] G. Paimard, E. Ghasali, M. Baeza, Screen-Printed Electrodes: fabrication, Modification, and Biosensing Applications, Chemosensors 11 (2023) 113, https://doi.org/10.3390/chemosensors11020113.
[19] E.B. Secor, Principles of aerosol jet printing, Flex. Print. Electron. 3 (2018) 035002, https://doi.org/10.1088/2058-8585/aace28.
[20] Y. Gu, D.R. Hines, V. Yun, M. Antoniak, S. Das, Aerosol-jet printed fillets for well-formed electrical connections between different leveled surfaces, Adv. Mater. Technol. 2 (2017) 1700178, https://doi.org/10.1002/admt.201700178.
[21] E.B. Secor, N.S. Bell, M.P. Romero, R.R. Tafoya, T.H. Nguyen, T.J. Boyle, Titanium hydride nanoparticles and nanoinks for aerosol jet printed electronics, Nanoscale 14 (2022) 12651–12657, https://doi.org/10.1039/D2NR03571E.
[22] G. Tarabella, D. Vurro, S. Lai, P. D'Angelo, L. Ascari, S. Iannotta, Aerosol jet printing of PEDOT:PSS for large area flexible electronics, Flex. Print. Electron. 5 (2020) 014005, https://doi.org/10.1088/2058-8585/ab61c4.
[23] R. Sajapin, D. Vurro, P. D'Angelo, G. Tarabella, S. Marasso, M. Cocuzza, M. Botti, M. Buttrini, A. Calderaro, T. Berzina, S. Iannotta, Aerosol jet printed organic memristive microdevices based on a chitosan: PANI composite conductive channel, ACS Appl. Electron. Mater. 4 (2022) 5875–5883, https://doi.org/10.1021/acsaelm.2c01047 (n.d.).
[24] E. Cantù, S. Tonello, G. Abate, D. Uberti, E. Sardini, M. Serpelloni, Aerosol jet printed 3D electrochemical sensors for protein detection, Sensors 18 (2018) 3719, https://doi.org/10.3390/s18113719.
[25] H. Yang, M.T. Rahman, D. Du, R. Panat, Y. Lin, 3-D printed adjustable microelectrode arrays for electrochemical sensing and biosensing, Sens. Actuat., B Chem. 230 (2016) 600–606, https://doi.org/10.1016/j.snb.2016.02.113.
[26] D. Majak, J. Fan, S. Kang, M. Gupta, Delta-9-tetrahydrocannabinol (Δ 9 -THC) sensing using an aerosol jet printed organic electrochemical transistor (OECT), J. Mater. Chem. B 9 (2021) 2107–2117, https://doi.org/10.1039/D0TB02951C.
[27] P. D'Angelo, M. Barra, P. Lombari, A. Coppola, D. Vurro, G. Tarabella, S. L. Marasso, M. Borriello, F. Chianese, A.F. Perna, A. Cassinese, D. Ingrosso, Homocysteine solution-induced response in aerosol jet printed OECTs by means of gold and platinum gate electrodes, Int. J. Mol. Sci. 22 (2021) 11507, https://doi.org/10.3390/ijms222111507.
[28] M.A.T. Gilmartin, J.P. Hart, Development of one-shot biosensors for the measurement of uric acid and cholesterol, Anal. Proc. Incl. Anal. Commun. 32 (1995) 341–345, https://doi.org/10.1039/AI9953200341.
[29] K. Duarte, C.I.L. Justino, A.C. Freitas, A.M.P. Gomes, A.C. Duarte, T.A.P. Rocha-Santos, Disposable sensors for environmental monitoring of lead, cadmium and mercury, TrAC - Trend. Anal. Chem. 64 (2015) 183–190, https://doi.org/10.1016/j.trac.2014.07.006.
[30] T. Vandenryt, B. Van Grinsven, K. Eersels, P. Cornelis, S. Kholwadia, T.J. Cleij, R. Thoelen, W. De Ceuninck, M. Peeters, P. Wagner, Single-shot detection of neurotransmitters in whole-blood samples by means of the heat-transfer method in combination with synthetic receptors, Sensors (Switzerland) (2017) 17, https://doi.org/10.3390/s17122701.
[31] D. Mabey, R.W. Peeling, A. Ustianowski, M.D. Perkins, Diagnostics for the developing world, Nat. Rev. Microbiol. 2 (2004) 231–240, https://doi.org/10.1038/nrmicro841.
[32] M. Gaboardi, R. Tatti, G. Bertoni, G. Magnani, R.D. Pergola, L. Aversa, R. Verucchi, D. Pontiroli, M. Riccò, Platinum carbonyl clusters decomposition on defective graphene surface, Surf. Sci. 691 (2020) 121499, https://doi.org/10.1016/j.susc.2019.121499.
[33] L. Tsui, S.C. Kayser, S.A. Strong, J.M. Lavin, High resolution aerosol jet printed components with electrodeposition-enhanced conductance, ECS J. Solid State Sci. Technol. 10 (2021) 047001, https://doi.org/10.1149/2162-8777/abf294.
[34] K.R. Bhattarai, H.-R. Kim, H.-J. Chae, Compliance with saliva collection protocol in healthy volunteers: strategies for managing risk and errors, Int. J. Med. Sci. 15 (2018) 823–831, https://doi.org/10.7150/ijms.25146.
[35] L. Fabbrizzi, The ferrocenium/ferrocene couple: a versatile redox switch, ChemTexts 6 (2020) 22, https://doi.org/10.1007/s40828-020-00119-6.
[36] F. Tuinstra, J.L. Koenig, Raman spectrum of graphite, J. Chem. Phys. 53 (1970) 1126–1130, https://doi.org/10.1063/1.1674108.

[37] G. Chen, Y. Gu, H. Tsang, D.R. Hines, S. Das, The effect of droplet sizes on overspray in aerosol-jet printing, Adv. Eng. Mater. (2018) 20, https://doi.org/10.1002/adem.201701084.
[38] M. Smith, Y.S. Choi, C. Boughey, S. Kar-Narayan, Controlling and assessing the quality of aerosol jet printed features for large area and flexible electronics, Flex. Print. Electron. 2 (2017) 015004, https://doi.org/10.1088/2058-8585/aa5af9.
[39] M. Acik, Y.J. Chabal, A review on reducing graphene oxide for band gap engineering, J. Mater. Sci. Res. 2 (2012) 101–112, https://doi.org/10.5539/jmsr.v2n1p101.
[40] C. Botas, P. Álvarez, C. Blanco, R. Santamaría, M. Granda, M.D. Gutiérrez, F. Rodríguez-Reinoso, R. Menéndez, Critical temperatures in the synthesis of graphene-like materials by thermal exfoliation-reduction of graphite oxide, Carbon N. Y. 52 (2013) 476–485, https://doi.org/10.1016/j.carbon.2012.09.059.
[41] A. Mezzi, S. Kaciulis, Surface investigation of carbon films: from diamond to graphite, Surf. Interface Anal. 42 (2010) 1082–1084, https://doi.org/10.1002/sia.3348.
[42] D. Pontiroli, M. Aramini, M. Gaboardi, M. Mazzani, S. Sanna, F. Caracciolo, P. Carretta, C. Cavallari, S. Rols, R. Tatti, L. Aversa, R. Verucchi, M. Riccò, Tracking the hydrogen motion in defective graphene, J. Phys. Chem. C 118 (2014) 7110–7116, https://doi.org/10.1021/jp408339m.
[43] D. Briggs, G. Beamson, Primary and secondary oxygen-induced C1s binding energy shifts in x-ray photoelectron spectroscopy of polymers, Anal. Chem. 64 (1992) 1729–1736, https://doi.org/10.1021/ac00039a018.
[44] M.J.E. Fischer, Amine coupling through EDC/NHS: a practical approach, Method. Mol. Biol. (2010) 55–73, https://doi.org/10.1007/978-1-60761-670-2_3.
[45] S. Stefansson, H.H. Kwon, S.N. Ahn, Targeting antibodies to carbon nanotube field effect transistors by pyrene hydrazide modification of heavy chain carbohydrates, J. Nanotechnol. 2012 (2012) 490175, https://doi.org/10.1155/2012/490175.
[46] A.C. Lazanas, M.I. Prodromidis, Electrochemical impedance spectroscopy-a tutorial, ACS Meas. Sci. Au 3 (2023) 162–193, https://doi.org/10.1021/acsmeasuresciau.2c00070.
[47] D. Gentili, P. D'Angelo, F. Militano, R. Mazzei, T. Poerio, M. Brucale, G. Tarabella, S. Bonetti, S.L. Marasso, M. Cocuzza, L. Giorno, S. Iannotta, M. Cavallini, Integration of organic electrochemical transistors and immuno-affinity membranes for label-free detection of interleukin-6 in the physiological concentration range through antibody-antigen recognition, J. Mater. Chem. B 6 (2018) 5400–5406, https://doi.org/10.1039/c8tb01697f.
[48] A. Diouf, B. Bouchikhi, N. El Bari, A nonenzymatic electrochemical glucose sensor based on molecularly imprinted polymer and its application in measuring saliva glucose, Mater. Sci. Eng. C 98 (2019) 1196–1209, https://doi.org/10.1016/j.msec.2019.01.001.
[49] P. Van Hao, C.T. Xuan, P.D. Thanh, N.-T. Thuat, N.H. Hai, M.A. Tuan, Detection analysis limit of nonlinear characteristics of DNA sensors with the surface modified by polypyrrole nanowires and gold nanoparticles, J. Sci. Adv. Mater. Devices 3 (2018) 129–138, https://doi.org/10.1016/j.jsamd.2018.04.002.
[50] S. Boonkaew, S. Chaiyo, S. Jampasa, S. Rengpipat, W. Siangproh, O. Chailapakul, An origami paper-based electrochemical immunoassay for the C-reactive protein using a screen-printed carbon electrode modified with graphene and gold nanoparticles, Microchim. Acta 186 (2019) 153, https://doi.org/10.1007/s00604-019-3245-8.
[51] Q. Xu, G. Wang, M. Zhang, G. Xu, J. Lin, X. Luo, Aptamer based label free thrombin assay based on the use of silver nanoparticles incorporated into self-polymerized dopamine, Microchim. Acta 185 (2018) 253, https://doi.org/10.1007/s00604-018-2787-5.
[52] H.P. Loock, P.D. Wentzell, Detection limits of chemical sensors: applications and misapplications, Sens. Actuat. B Chem. 173 (2012) 157–163, https://doi.org/10.1016/j.snb.2012.06.071.